The Astrophysical Journal, 909:164 (10pp), 2021 March 10 https://doi.org/10.3847/1538-4357/abdbb6

Supervirial Temperature or Neon Overabundance? Suzaku Observations of the Milky Way Circumgalactic Medium

Anjali Gupta[1,2], Joshua Kingsbury[1], Smita Mathur[2,3], Sanskriti Das[2], Massimiliano Galeazzi[4], Yair Krongold[5], and Fabrizio Nicastro[6]

[1] Columbus State Community College, 550 East Spring Street, Columbus, OH 43215, USA; agupta1@cscc.edu
[2] Department of Astronomy, The Ohio State University, 140 West 18th Avenue, Columbus, OH 43210, USA
[3] Center for Cosmology and Astroparticle Physics, 191 West Woodruff Avenue, Columbus, OH 43210, USA
[4] Physics Department, University of Miami, Coral Gables, FL 33155, USA
[5] Instituto de Astronomia, Universidad Nacional Autonoma de Mexico, 04510 Mexico City, Mexico
[6] Observatorio Astronomico di Roma-INAF, Via di Frascati 33, 1-00040 Monte Porzio Catone, RM, Italy
Received 2020 October 8; revised 2021 January 10; accepted 2021 January 12; published 2021 March 15

Abstract

We analyzed Suzaku and Chandra observations of the soft diffuse X-ray background toward four sight lines with the goal of characterizing the X-ray emission from the Milky Way circumgalactic medium (CGM). We identified two thermal components of the CGM, one at a uniform temperature of $kT = 0.176 \pm 0.008$ keV and the other at temperatures in the range $kT = 0.65$–0.90 keV. The uniform lower-temperature component is consistent with the Galaxy's virial temperature ($\sim 10^6$ K). The temperatures of the hotter components are similar to that recently discovered ($\sim 10^7$ K) in the sight line to blazar 1ES 1553+113, passing close to the Fermi bubble. Alternatively, the spectra can be described by just one lower-temperature component with supersolar neon abundance, once again similar to that found in the 1ES 1553+113 sight line. The additional hot component or the overabundance of Ne is required at a significance of $>4\sigma$, but we cannot distinguish between the two possibilities. These results show that the supervirial temperature gas or an enhanced Ne abundance in the warm-hot gas in the CGM is widespread, and these are not necessarily related to the Fermi bubble.

Unified Astronomy Thesaurus concepts: Circumgalactic medium (1879)

1. Introduction

The circumgalactic medium (CGM) is an important component of a spiral galaxy. The CGM is defined as the gaseous medium surrounding the stellar disk of a galaxy extended out to its virial radius. It serves as a gas reservoir with accretion from the intergalactic medium and outflows from the stellar disk (star formation and/or active galactic nucleus induced). Some of this material may recycle back into the disk of the galaxy, while some may stay in the diffuse CGM. This helps to regulate the formation and evolution of a galaxy. The CGM is also believed to contain more baryonic mass than the entire stellar disk, as well as most of the metals produced by stars (White & Rees 1978; Oppenheimer et al. 2016; Nelson et al. 2018). Thus, the CGM may harbor the largest galactic baryon and metal reservoir. The CGM is predicted to be predominantly warm-hot, $T \approx 10^5$–10^7 K, with most of the baryons in the hotter $T \approx 10^6$–10^7 K phase (Stinson et al. 2012).

The higher-temperature ($\geqslant 10^6$ K) phases of the CGM can only be probed by soft X-ray observations, particularly the oxygen transitions of O VII and O VIII, both in absorption and emission. Because of our special vantage point, our own Milky Way provides a unique opportunity to probe the CGM of a spiral galaxy. Absorption lines due to O VII and O VIII at redshift zero from the Milky Way CGM have been detected toward extragalactic sight lines by Chandra and XMM-Newton (Nicastro et al. 2002; Wang et al. 2005; Williams et al. 2005, 2006a, 2006b, 2007; Gupta et al. 2012, 2014; Fang et al. 2019). The line ratios of O VII/O VIII constrain the absorbing gas temperature in the range of (0.1–0.2) keV (1.2–2.5×10^6 K), assuming both absorption lines arise in the same plasma (Gupta et al. 2012).

Various broadband X-ray observations have revealed an extensive soft ($\sim$0.1–1.0 keV) diffuse X-ray background (SDXB; Snowden et al. 1998, 2000). The "shadow observations," in which the X-ray emission toward a molecular cloud at a known distance is compared with a nearby line of sight with low absorption, show that there is a significant contribution from the Milky Way CGM to the SDXB (Smith et al. 2007; Galeazzi et al. 2009; Gupta et al. 2009; Henley & Shelton 2015). Several studies have attempted to measure the Galactic CGM contribution to the SDXB using XMM-Newton and Suzaku observations of empty fields (with no bright source in the field of view; Yoshino et al. 2009; Henley et al. 2010; Henley & Shelton 2013; Nakashima et al. 2018). All of these X-ray emission studies of the warm-hot gas in the Galactic halo[7] have shown that the gas temperature is fairly constant across the sky, 0.15–0.21 keV (1.8–2.4×10^6 K), and comparable to the absorbing gas temperature.

Although X-ray emission and absorption observations established the presence of the warm-hot gas in the Galactic halo, the extent, density, and mass of this warm-hot gas has been a matter of debate. Determining the density (n_e) and path length (R) of the warm-hot gas is critical for estimating its total baryonic mass. However, this is difficult in part due to the insufficiency of current X-ray gratings to resolve the absorption lines, and also because of the degeneracy involved in using absorption or emission studies alone. The strength of an absorption line depends on the ionic column density, which in turn depends on the equivalent hydrogen density ($N_{\rm H} = \int n_H dr$) of the intervening gas, while the emission measure (EM) is sensitive to the square of the electron number density (EM $= \int n_{\rm e}^2 dr$). Combining absorption and emission measurements breaks the degeneracy and provides

[7] Different fields have traditionally used different nomenclature to describe the gas filling the Galactic halo. We will therefore use the terms "CGM" and "halo" interchangeably.

Table 1
Suzaku and Chandra Observation Log

Target	l	b	Suzaku			Chandra		
			ObsID	Start Date	Exposure (ks)	ObsID	Start Date	Exposure (ks)
	(deg)	(deg)						
Off-field 2	37.42	−30.55	509043010	2014 May 7	80.16	...	...	...
Off-field 3	91.73	−24.10	509044010	2014 June 11	97.33	21380	2019 July 14	9.45
Off-field 4	286.33	+23.55	509045010	2014 Dec 17	81.32	21381	2018 Nov 29	9.94
Off-field 5	39.92	−36.21	509046010	2014 May 10	80.91	21382	2018 Nov 8	9.95

constraints on the path length and density of the absorbing/emitting plasma.

In our previous work (Gupta et al. 2012), comparing the absorption and emission values averaged over the whole sky, we found that there is a huge reservoir of ionized gas in the Galactic halo with a mass of over $\sim 6 \times 10^{10}\, M_{\odot}$ and a radius of over 100 kpc. However, shadow observations and other studies of the SDXB show that the EM of the Galactic halo varies by an order of magnitude in different sight lines (Yoshino et al. 2009; Henley & Shelton 2013, 2015; Nakashima et al. 2018). This large variation critically affects estimates of the path length of the warm-hot gas and, subsequently, the mass measurements. Therefore, it is essential to measure the X-ray emission of the warm-hot gas close to the absorption sight line (Gupta et al. 2014, 2017).

With the goal to determine the X-ray emission properties of the Milky Way CGM near absorption sight lines of Mrk 509, Ark 564, NGC 3783, and H2106-099 (from Gupta et al. 2012), we observed with Suzaku four empty fields close to these sight lines for 80 ks each (PI: Gupta). We also observed three of the Suzaku fields with Chandra to identify the point sources contaminating the diffuse X-ray emission (PI: Gupta). In this paper, we report on the analysis of our Chandra (Section 2) and Suzaku (Section 3) observations. In Section 4, we present our results from the spectral analysis; we show that, in addition to the gas close to the virial temperature, a supervirial temperature component or an enhanced Ne abundance is required. Our discussion is presented in Section 5, and we conclude in Section 6.

2. Chandra Observations and Point-source Detection

Even in "empty" fields, point sources add a significant contribution to the truly diffuse emission; hence, it is necessary to exclude them. Unfortunately, the poor angular resolution of Suzaku makes any significant point-source identification impossible. We observed the Suzaku fields Off-field 3, Off-field 4, and Off-field 5 with Chandra for ∼10 ks each to identify the point sources. The observation IDs, dates, and exposure times are summarized in Table 1. Off-field 2, close to the Mrk 509 sight line, was observed with XMM-Newton in 2014; for this field, we identified the point sources from the XMM-Newton observation. A detailed analysis of the XMM-Newton Off-field 2 observation is given in Gupta et al. (2017).

All of the Chandra analysis was performed with the software Chandra Interactive Analysis of Observations (CIAO 4.12).[8] We reprocessed the Chandra data with the *repro* script to apply standard corrections. We also filtered the data sets for bad time intervals affected by flares. We generated 0.5–2.0 keV images and the corresponding exposure maps. We used the *wavdetect* tool to identify the point sources in the images. We identified 14, 13, and 9 X-ray point sources in the Off-field 3, Off-field 4, and Off-field 5 images, respectively, down to a detection limit of 5.3×10^{-15} erg cm^{-2} s^{-1}. In the Suzaku field Off-field 2, we identified 23 point sources using the XMM-Newton observation, with a detection limit of 2.6×10^{-15} erg cm^{-2} s^{-1}. Our number of identified point sources is well in agreement with the log N–log S in the Chandra Deep Field South (CDFS; Lehmer et al. 2012).

3. Suzaku Observations and Data Reduction

In this work, we only used data from the back-illuminated X-ray Imaging Spectrometer (XIS-1), featuring the largest effective area among all Suzaku detectors at soft X-ray energies (0.3–5.0 keV). The Suzaku observation IDs, dates, pointing directions, and exposure times are summarized in Table 1.

For data reduction, we followed the procedures described in the Suzaku Data Reduction Guide.[9] In addition to standard data processing, we performed data screening with the cutoff rigidity (COR) of the Earth's magnetic field, which varies as Suzaku traverses its orbit. During times with larger COR values, fewer particles are able to penetrate the satellite and the XIS detectors. We excluded times when the COR was less than 8 GV, which is greater than the default value of 2 GV. This helps to lower the particle background.

Our goal is to extract the spectrum of the diffuse emission. Therefore, we first removed the point sources identified in the Chandra and XMM-Newton observations and then extracted the spectrum from the entire field of view. Since Suzaku has a broad point-spread function (half-power diameter ∼2′), we excised regions within a 1′ radius of the point-source locations from the Suzaku fields. For sources too bright to be adequately removed by this region, we selected larger source exclusion radii by eye of the order of 2′–3′.

We produced the redistribution matrix files using the *xisrmfgen* ftool, in which the degradation of the energy resolution and its position dependence are included. We also prepared ancillary response files (ARFs) using the *xissimarfgen* ftool with the revised recipe.[10] For the ARF calculations, we assumed a uniform source of radius 20′ and used a detector mask that removed the bad pixel regions. We estimate the total instrumental background from the database of the night Earth data with the *xisnxbgen* ftool.

4. Spectral Analysis

4.1. Milky Way CGM Emission

The goal of this study is to constrain the properties of the Milky Way CGM. We isolated the Milky Way CGM from the different components of the SDXB (empty field spectrum) by

[8] https://cxc.harvard.edu/ciao/

[9] https://heasarc.gsfc.nasa.gov/docs/suzaku/analysis/abc/

[10] https://heasarc.gsfc.nasa.gov/docs/suzaku/analysis/xisnxbnew.html

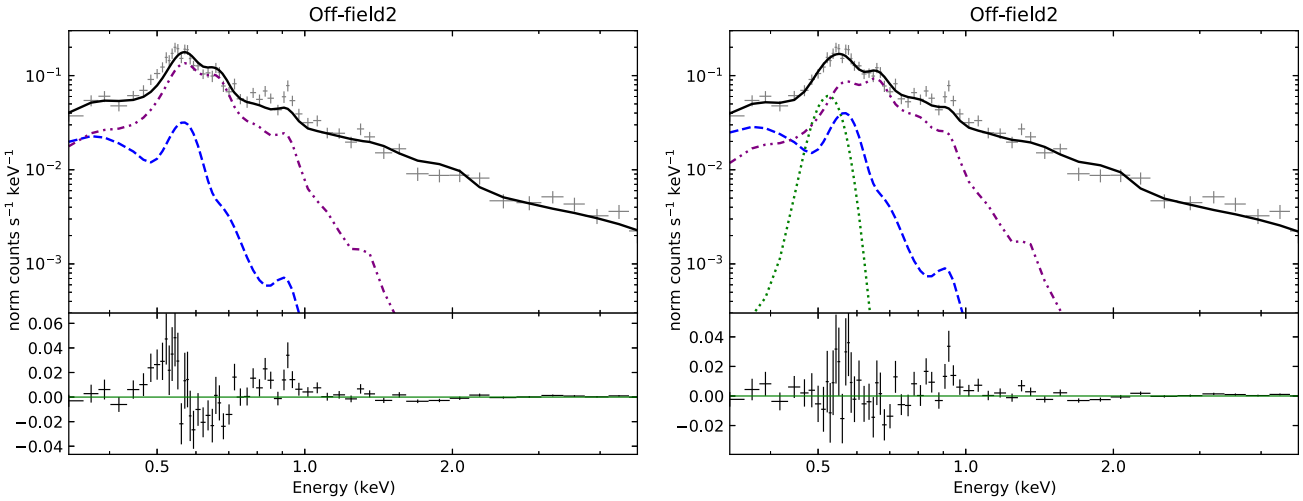

Figure 1. Left: Off-field 2 Suzaku XIS1 spectrum with the standard SDXB three-component best-fit model. Excess emission near 0.5 keV can be clearly seen in the residual plot. Right: SDXB three-component model plus a Gaussian line accounting for the O I emission. The blue curve shows the foreground spectrum, and the purple curve shows the spectrum of the Milky Way CGM in the warm-hot phase.

spectral analysis. This was a challenging task, as the SDXB has contributions from different sources, such as the Solar Wind Charge eXchange (SWCX), the Local Bubble (LB), the cosmic X-ray background (CXB) made of unresolved point sources, and the Milky Way CGM itself.

Therefore, a typical SDXB spectrum is described by a three-component model: (1) a foreground component consisting of the LB and SWCX, modeled as an unabsorbed thermal plasma emission in collisional ionization equilibrium (CIE) with a temperature of $kT = 0.1$ keV (Gupta et al. 2009; Henley & Shelton 2013; Liu et al. 2017); (2) a background component of CXB, modeled with an absorbed power law; and (3) the Milky Way CGM component, modeled as an equilibrium thermal plasma absorbed by the cold gas in the Galactic disk. We performed all of the spectral fitting with Xspec version 12.10.1f.[11] We modeled all of the thermal plasma components in CIE with the APEC (version 3.0.9) model (Smith et al. 2001) and used the solar relative metal abundances of Anders & Grevesse (1989). For absorption by the Galactic disk, we used the *phabs* model in XSPEC.

Initially, we fit the Suzaku XIS-1 spectra with the standard SDXB three-component model [$\mathrm{apec_{(LB+SWCX)}} + \mathrm{phabs} \times (\mathrm{apec_{Halo}} + \mathrm{powerlaw_{CXB}})$]. The temperature of the foreground component was frozen at $kT = 0.1$ keV, but we allowed the normalization to vary. We fixed the total metallicity to 1 (in solar units) for both thermal components, as there is a strong correlation between the total metallicity and normalizations (or EM). The Galactic column densities were fixed to values determined from Dickey & Lockman (1990). We fixed the power-law photon index to 1.52 and left the normalization as a free parameter in the spectral fits (Table 3). After fitting the spectra (in the energy range of 0.3–5.0 keV) with the three-component model as described above, we noted a significant excess in the data around 0.50–0.55 keV in all four spectra (Figure 1). We also noted excess emission near 0.8–1.0 keV in Off-field 2, Off-field 3, and Off-field 5 (Figure 2). We attempted to fit these excess emissions as discussed below.

[11] https://heasarc.gsfc.nasa.gov/xanadu/xspec/

4.1.1. O I Contamination in Suzaku Data

Sekiya et al. (2014) noted that the Suzaku observations, particularly after 2011, were affected by the increase in the solar activity. The enhanced interaction of solar X-rays with the neutral oxygen in the Earth's atmosphere creates an O I fluorescent line at $E = 0.525$ keV and contaminates the Suzaku spectra. The Suzaku XIS cannot distinguish the O I line from the O VII Kα triplet (561, 569, and 574 eV, centroid at 571 eV) owing to its energy resolution of ≈50 eV. Unless the O I fluorescent line is taken into account in the spectral analysis, the O VII line intensity would be overestimated.

Since all of the observations in this study were taken in 2014, the excess near 0.50–0.55 keV could be due to the O I fluorescent line. To investigate the effect of the O I contamination, we measured the intensity of the oxygen emission lines. We modified the above three-component model by switching the APEC thermal plasma component to VAPEC, which allows for variable elemental abundances. We fixed the oxygen abundance to zero, thereby removing the oxygen contribution from the model. We then added three Gaussian lines at the energies of the O I (525 eV), O VII Kα triplet (centroid at 571 eV), and O VIII (665 eV) lines and fitted the spectra again. Table 2 reports the best-fit oxygen line intensities. Note that O I has a significant contribution in all spectra ranging from 2.3 to 20.7 photons s^{-1} cm^{-2} sr^{-1} (L.U.). This is about 25%–130% of the O VII intensity in the four spectra.

The O I contamination can be minimized by choosing the events taken during time intervals when the elevation angle from the bright Earth limb (DYE_ELV parameter) is greater than 60° (Sekiya et al. 2014). However, this results in the loss of a large amount of data. To further investigate the O I contamination, we compared the O I line intensity for DYE_ELV > 20°, >40°, and >60° in our observations (Table 2). Off-field 4 had unusually high O I emission (20.75 ± 1.38 L.U.) for the DYE_ELV > 20° selection, but with DYE_ELV > 40°, the O I emission was significantly reduced. With DYE_ELV > 40°, the O I emission was reduced to 6%–40% of the O VII intensity. Therefore, instead of restricting the data filtered only for DYE_ELV > 60°, for further analysis, we used DYE_ELV > 40°; we took care of the residual O I contamination by adding a Gaussian line to our spectral model. This resulted in a good balance between optimizing the effective exposure time and mitigating the O I contamination. As

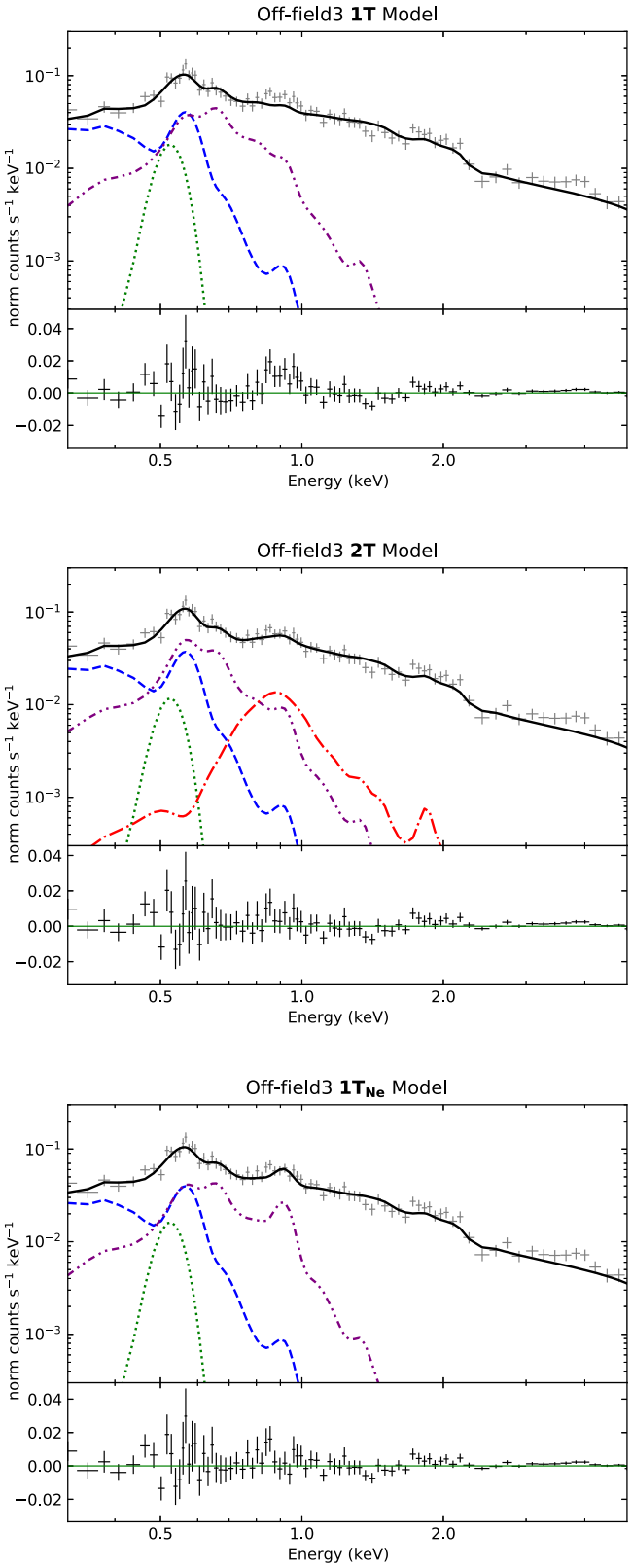

Figure 2. Off-field 3 spectral fits. Top: data fitted with the 1*T* model; note the excess near 0.9 keV. Middle: 2*T* model fit; the excess emission is modeled as an additional hot thermal component. Bottom: $2T_{\rm Ne}$ model fit; the excess emission is modeled as an Ne emission line.

discussed in the next section, the use of DYE_ELV $> 40°$ instead of the more stringent limit of DYE_ELV $> 60°$ has not caused any bias in our measurements.

4.1.2. One-temperature (1T) CGM Model

We refitted the Suzaku XIS-1 spectra with the standard SDXB three-component model plus a Gaussian line to account for the O I emission. We call this model the one-temperature (1*T*) CGM model. Figure 1 shows the best-fit 1*T* model for Off-field 2.

As noted above, we used data with DYE_ELV $> 40°$ to optimize the exposure time and thus obtain tighter constraints on the fit statistics. To further verify that this choice is not introducing any bias in our analysis, we also fitted the 1*T* model to data sets filtered with DYE_ELV $> 20°$ and $>60°$. Table 3 reports the best-fit 1*T* model parameters for DYE_ELV $> 20°$, $>40°$, and $>60°$ for our observations. The best-fit parameters are consistent within the uncertainties, and DYE_ELV $> 40°$ provides better fit statistics, especially for Off-field 4 and Off-field 5.

The temperatures of the Galactic CGM (absorbed thermal component) among all fields are consistent with each other within the uncertainties, with an average value of $kT = 0.195 \pm 0.007$ keV, close to the Galaxy's virial temperature. The EMs vary in the $(5.7–14.3) \times 10^{-3}$ cm^{-6} pc range (Table 3); these EMs are very high, well above the typical values reported by previous studies (we discuss this in detail in Section 5).

In our 1*T* spectral model, the CXB from unresolved extragalactic sources is modeled with an absorbed power law with a fixed photon index of 1.52. The best-fit normalizations at 1 keV are in the range of 8.7–13.2 photons keV^{-1} s^{-1} sr^{-1} cm^{-2} (Table 3). Cappelluti et al. (2017), using Chandra deep observations of the COSMOS field, provided one of the most accurate measurements of the CXB. They measured the 1 keV normalization of the CXB power law of 10.91 ± 0.16 photons keV^{-1} s^{-1} sr^{-1} cm^{-2}. The power-law normalizations in our observations are in the same range as the COSMOS field and other previous Suzaku and XMM-Newton studies of the SDXB (Galeazzi et al. 2009; Gupta et al. 2009; Nakashima et al. 2018). Thus, our results are not biased by the fit to the CXB component.

We modeled the foreground emission of the LB and SWCX as an unabsorbed plasma in CIE with thermal emission. We fixed the temperature of this component to $kT = 0.1$ keV and measured the best-fit EMs in the range of 0.015–0.018 cm^{-6} pc toward our four fields (Table 3). To determine what fraction of the foreground emission is due to the SWCX, which is a time-variable component, we first estimated the LB emission using the maps in Liu et al. (2017). They generated all-sky maps of the LB temperature and EM using the ROSAT All Sky Survey data corrected for the SWCX. In the Liu et al. maps, the LB EMs are near $\sim$0.001 cm^{-6} pc toward Off-field 2, Off-field 3, and Off-field 5 and $\sim$0.003 cm^{-6} pc toward Off-field 4. The LB EMs are much lower than our measured values of foreground EMs of 0.015–0.018 cm^{-6} pc, clearly showing a high contribution from the SWCX. However, this is not unexpected, as our observations were made during 2014, which was a period of high solar activity. Some of the previous studies of the SDXB have also measured such large EMs for the foreground component (Gupta et al. 2009; Henley & Shelton 2015; Nakashima et al. 2018). Henley & Shelton (2015) well constrained the foreground component EMs in the range of 0.005–0.079 (for Anders & Grevesse 1989 abundances) using the Suzaku and XMM-Newton shadow observations, bracketing our values. Thus, our results do not seem to be biased by the fit to the foreground components either.

We used our fit results of the foreground (unabsorbed APEC) component to obtain O VII and O VIII line intensities from the LB and SWCX. We measured total O VII line intensities from the LB plus SWCX of 5.89 ± 1.55,

Table 2
Oxygen Emission Line Intensities

Data Set	Exposure (s)	O_{VII} L.U.	O_{VIII} L.U.	O_I L.U.	χ^2/dof
Off-field 2					
DYE_ELV > 20°	53,580	16.79 ± 2.16	5.70 ± 0.95	5.86 ± 1.42	195.3/202
DYE_ELV > 40°	47,609	17.08 ± 2.25	5.59 ± 0.96	3.12 ± 1.68	178.8/177
DYE_ELV > 60°	44,147	17.55 ± 2.35	5.67 ± 1.02	2.31 ± 1.75	162.7/164
Off-field 3					
DYE_ELV > 20°	79,816	9.31 ± 1.29	2.25 ± 0.58	2.34 ± 0.89	321.3/329
DYE_ELV > 40°	72,709	8.59 ± 1.30	2.33 ± 0.57	1.37 ± 1.04	310.6/301
DYE_ELV > 60°	63,240	8.58 ± 1.37	2.45 ± 0.62	0.68 ± 0.85	277.6/269
Off-field 4					
DYE_ELV > 20°	62,975	16.04 ± 1.63	2.58 ± 0.63	20.75 ± 1.38	378.0/328
DYE_ELV > 40°	44,121	10.75 ± 1.66	3.49 ± 0.70	4.25 ± 1.21	252.0/238
DYE_ELV > 60°	30,026	10.19 ± 1.85	3.20 ± 0.83	0.52 ± 0.85	169.0/153
Off-field 5					
DYE_ELV > 20°	52,949	15.94 ± 1.85	4.18 ± 0.81	4.32 ± 1.10	268.8/245
DYE_ELV > 40°	45,449	13.96 ± 1.85	4.17 ± 0.83	0.89 ± 1.05	219.9/211
DYE_ELV > 60°	39,274	13.77 ± 1.98	4.43 ± 0.90	0.75 ± 1.00	226.2/183

Note. Normalization of Gaussian lines is in units of L.U. (photons s^{-1} cm^{-2} sr^{-1}).

Table 3
Best-fit Parameters: 1*T* Model

Target Data Set	O_I Norm.[a]	Foreground EM[b] (10^{-2} cm^{-6} pc)	N_H[c] 10^{20} cm^{-2}	Galactic Halo		Power-law Norm.[d]	χ^2/dof
				kT (keV)	EM (10^{-2} cm^{-6} pc)		
Off-field 2							
DYE_ELV > 20°	5.8 ± 1.4	1.84 ± 0.44	4.78	0.200 ± 0.012	1.41 ± 0.23	8.84 ± 0.54	212.9/205
DYE_ELV > 40°	3.2 ± 1.4	1.76 ± 0.46	”	0.199 ± 0.011	1.43 ± 0.25	8.84 ± 0.58	194.5/179
DYE_ELV > 60°	2.7 ± 1.5	1.80 ± 0.48	”	0.199 ± 0.011	1.48 ± 0.27	8.69 ± 0.60	181.6/167
Off-field 3							
DYE_ELV > 20°	2.9 ± 0.9	1.55 ± 0.29	3.76	0.200 ± 0.016	0.63 ± 0.16	13.02 ± 0.46	345.6/332
DYE_ELV > 40°	1.5 ± 0.9	1.55 ± 0.29	”	0.207 ± 0.018	0.57 ± 0.14	13.11 ± 0.49	324.5/304
DYE_ELV > 60°	0.6 ± 0.7	1.60 ± 0.32	”	0.204 ± 0.019	0.58 ± 0.16	13.21 ± 0.52	287.2/272
Off-field 4							
DYE_ELV > 20°	18.2 ± 1.7	1.67 ± 0.42	9.02	0.158 ± 0.014	2.03 ± 0.74	13.21 ± 0.46	436.8/331
DYE_ELV > 40°	2.6 ± 1.2	1.81 ± 0.36	”	0.183 ± 0.014	1.13 ± 0.32	12.64 ± 0.56	253.4/241
DYE_ELV > 60°	0.0 ± 0.0	1.66 ± 0.39	”	0.191 ± 0.014	1.03 ± 0.25	11.13 ± 0.64	173.6/156
Off-field 5							
DYE_ELV > 20°	3.2 ± 1.3	1.51 ± 0.41	5.24	0.185 ± 0.010	1.39 ± 0.29	10.85 ± 0.52	293.3/248
DYE_ELV > 40°	0.1 ± 0.4	1.63 ± 0.43	”	0.192 ± 0.011	1.18 ± 0.22	10.85 ± 0.57	232.6/214
DYE_ELV > 60°	0.0 ± 0.0	1.44 ± 0.44	”	0.191 ± 0.010	1.23 ± 0.21	10.75 ± 0.60	233.5/186

Notes.
[a] Normalization of the Gaussian at the fixed center energy $E = 0.525$ keV in units of L.U. (photons s^{-1} cm^{-2} sr^{-1}).
[b] The EM for the foreground (LB+SWCX) component with temperature fixed at $kT = 0.1$ keV.
[c] Galactic values of the absorption column density given in Dickey & Lockman (1990).
[d] Normalization of the power-law model with fixed photon index $\Gamma = 1.52$ in units of photons keV^{-1} s^{-1} sr^{-1} cm^{-2}.

5.20 ± 0.97, 6.05 ± 1.20, and 5.44 ± 1.43 L.U. toward Off-field 2, Off-field 3, Off-field 4 , and Off-field 5, respectively. The O VIII line intensities are 0.30 ± 0.08, 0.26 ± 0.05, 0.30 ± 0.06, and 0.27 ± 0.07 L.U. for Off-field 2, Off-field 3, Off-field 4 , and Off-field 5, respectively. The LB EMs from Liu et al. of 0.001–0.003 correspond to O VII and O VIII line

Table 4
$1T$, $2T$, and $1T_{\rm Ne}$ Model Fits: Individual Spectral Fits

Target/ Model	O_I Norm.[a]	Foreground EM[b] (10^{-2} cm^{-6} pc)	Galactic Halo					Power-law Norm.[f]	χ^2/dof
			kT_1[c] (keV)	EM_1 (10^{-2} cm^{-6} pc)	kT_2[d] (keV)	EM_2 (10^{-2} cm^{-6} pc)	Ne[e]		
Off-field 2									
$1T$[g]	3.2 ± 1.4	1.76 ± 0.46	0.199 ± 0.011	1.43 ± 0.25	...	...	...	8.84 ± 0.58	194.5/179
$2T$[h]	2.1 ± 1.7	1.49 ± 0.55	0.178 ± 0.016	1.74 ± 0.44	0.691 ± 0.152	0.082 ± 0.042	...	8.27 ± 0.65	184.0/177
$1T_{\rm Ne}$[i]	3.0 ± 1.5	1.75 ± 0.48	0.195 ± 0.011	1.46 ± 0.27	...	...	1.9 ± 0.5	8.65 ± 0.59	185.1/178
Off-field 3									
$1T$[g]	1.5 ± 0.9	1.55 ± 0.29	0.207 ± 0.018	0.57 ± 0.14	...	...	...	13.11 ± 0.49	324.5/304
$2T$[h]	1.0 ± 0.9	1.43 ± 0.32	0.178 ± 0.020	0.72 ± 0.25	0.799 ± 0.121	0.059 ± 0.024	...	12.45 ± 0.55	309.2/302
$1T_{\rm Ne}$[i]	1.3 ± 0.9	1.53 ± 0.30	0.197 ± 0.017	0.60 ± 0.16	...	...	2.9 ± 0.9	12.83 ± 0.49	308.9/303
Off-field 4									
$1T$[g]	2.6 ± 1.2	1.81 ± 0.36	0.183 ± 0.014	1.13 ± 0.32	...	...	...	12.64 ± 0.56	253.4/241
$2T$[h]	...	...	...	...	...	...	...	...	...
$1T_{\rm Ne}$[i]	2.6 ± 1.2	1.81 ± 0.40	0.181 ± 0.014	1.14 ± 0.33	...	...	1.3 ± 0.7	12.64 ± 0.57	252.9/240
Off-field 5									
$1T$[g]	0.1 ± 0.4	1.63 ± 0.43	0.192 ± 0.009	1.18 ± 0.22	...	...	...	10.85 ± 0.57	232.6/214
$2T$[h]	0.0 ± 0.0	1.48 ± 0.46	0.176 ± 0.012	1.34 ± 0.28	0.690 ± 0.125	0.060 ± 0.032	...	10.28 ± 0.63	223.7/212
$1T_{\rm Ne}$[i]	0.0 ± 0.0	1.61 ± 0.43	0.187 ± 0.010	1.22 ± 0.22	...	...	2.2 ± 0.7	10.66 ± 0.56	222.0/213

Notes.
[a] Normalization of the Gaussian at the fixed center energy $E = 0.525$ keV in units of L.U. (photons s^{-1} cm^{-2} str^{-1}).
[b] The EM for the foreground (LB+SWCX) component with temperature fixed at $kT = 0.1$ keV.
[c] Temperature of the Galactic halo warm-hot phase thermal component.
[d] Temperature of the Galactic halo hot phase thermal component.
[e] The Ne abundance for the Galactic halo warm-hot phase component.
[f] Normalization of the power-law model with fixed photon index $\Gamma = 1.52$ in units of photons keV^{-1} s^{-1} sr^{-1} cm^{-2}.
[g] Galactic halo one-temperature model.
[h] Galactic halo two-temperature model.
[i] Galactic halo one-temperature model with variable Ne abundance.

intensities of 0.33–1.00 and 0.02–0.06 L.U. Subtracting the LB emission from the total foreground line intensities can provide an estimate of the contribution from the SWCX O VII and O VIII line emission. The estimated SWCX O VII and O VIII line intensities in our observations are in the range of ∼4.9–5.6 and ∼0.24–0.28 L.U.

4.1.3. Two-Temperature (2T) or Enhanced Ne Abundance ($1T_{Ne}$) CGM Models

After fitting the spectra with the $1T$ models, we found excess emission in the 0.8–1.0 keV range along three out of four sight lines (Figure 2). We attempted to model this excess emission in two different ways. First, we added another absorbed thermal component (APEC) to the $1T$ model; we refer to this as the two-temperature ($2T$) model. Thus, the $2T$ model is given by $\mathrm{apec_{LB+SWCX}} + phabs \times (\mathrm{apec_{Halo}} + \mathrm{apec_{Halo}} + \mathrm{powerlaw_{CXB}}) + \mathrm{gaussian_{OI}}$. Model fits to these three spectra were significantly better with the $2T$ model compared to the $1T$ model ($\Delta\chi^2/\Delta\mathrm{dof} = 10.5/2, 15.3/2$, and $8.9/2$ for the Off-field 2, Off-field 3, and Off-field 5 spectra, respectively). The additional thermal component is required at a significance of 99.1%, 99.9%, and 97.6% (F-test) for the Off-field 2, Off-field 3, and Off-field 5 spectra, respectively. The temperature of the warm-hot CGM is consistent within the errors with an average value of $kT = 0.177 \pm 0.009$ keV, and the EM is in the range 7.2–17.4 $\times 10^{-3}$ cm^{-6} pc (Table 4). The temperature of the second component ($kT =$ (0.6–0.9) keV) is much higher than the warm-hot phase; hereafter, we call this the hot component (Figure 2 and Table 4).

The hot component spectrum is peaked at ≈0.9 keV, close to the energy of the Ne IX forbidden line (0.92 KeV). Along with O VII and O VIII, Ne IX also probes the warm-hot (∼10^6 K) medium. Therefore, we tried to fit the spectra with the $1T$ model but replacing the APEC model with VAPEC with variable Ne abundance (we call this the $1T_{\rm Ne}$ model); abundances of other elements were fixed at solar abundances as before (Yoshino et al. 2009; Mitsuishi et al. 2012). This model also showed a similar improvement in the fit statistics ($\Delta\chi^2/\Delta\mathrm{dof} = 9.4/1$, $15.6/1$, and $10.6/1$ for the Off-field 2, Off-field 3, and Off-field 5 spectra, respectively; Table 4). The Ne overabundance is required at a significance of 99.6%, 99.9%, and 99.8% (F-test) for the Off-field 2, Off-field 3, and Off-field 5 spectra, respectively. The temperature of the warm-hot CGM in the three fields is similar within the uncertainties with an average value of $kT = 0.190 \pm 0.007$ keV, the EM is in the range (6.0–14.6) $\times 10^{-3}$ cm^{-6} pc, and the Ne abundances are in the range of 1.4–3.8 times solar (Table 4).

4.1.4. Simultaneous Fit

The temperature of the warm-hot component was found to be consistent within the errors among all fields ($kT_1 \approx 0.2$ keV;

Table 5
$1T$, $2T$, and $1T_{\rm Ne}$ Model Fits: Simultaneous Spectral Fits

Model/ Target	O_I Norm.[a]	Foreground EM[b] (10^{-2} cm^{-6} pc)	Galactic Halo					Power-law Norm.[f]	χ^2/dof
			kT_1[c] (keV)	EM_1 (10^{-2} cm^{-6} pc)	kT_2[d] (keV)	EM_2 (10^{-2} cm^{-6} pc)	Ne[e]		
$1T$[g]									
Off-field 2	3.1 ± 1.3	1.72 ± 0.41	0.198 ± 0.007	1.45 ± 0.18	⋯	⋯	⋯	8.89 ± 0.57	1000.9/937
Off-field 3	1.2 ± 0.8	1.47 ± 0.25	”	0.65 ± 0.10	⋯	⋯	⋯	13.17 ± 0.47	”
Off-field 4	3.3 ± 1.0	2.00 ± 0.30	”	0.92 ± 0.15	⋯	⋯	⋯	12.57 ± 0.55	”
Off-field 5	0.4 ± 0.7	1.75 ± 0.36	”	1.15 ± 0.15	⋯	⋯	⋯	10.78 ± 0.55	”
$2T$[h]									
Off-field 2	2.1 ± 1.4	1.51 ± 0.47	0.176 ± 0.008	1.80 ± 0.29	0.703 ± 0.117	0.10 ± 0.04	⋯	8.27 ± 0.62	939.3/929
Off-field 3	1.0 ± 0.8	1.47 ± 0.29	”	0.78 ± 0.16	0.806 ± 0.089	0.09 ± 0.02	⋯	12.49 ± 0.54	”
Off-field 4	2.5 ± 1.1	1.82 ± 0.34	”	1.23 ± 0.24	0.698 ± 0.339	0.04 ± 0.03	⋯	12.55 ± 0.61	”
Off-field 5	0.0 ± 0.0	1.62 ± 0.42	”	1.39 ± 0.21	0.715 ± 0.088	0.09 ± 0.03	⋯	10.31 ± 0.62	”
$1T_{\rm Ne}$[i]									
Off-field 2	3.0 ± 1.3	1.75 ± 0.43	0.195 ± 0.007	1.47 ± 0.20	⋯	⋯	1.9 ± 0.5	8.71 ± 0.58	956.3/933
Off-field 3	1.3 ± 0.8	1.52 ± 0.26	”	0.65 ± 0.11	⋯	⋯	3.1 ± 0.9	12.92 ± 0.48	”
Off-field 4	3.2 ± 1.0	1.98 ± 0.30	”	0.95 ± 0.16	⋯	⋯	1.5 ± 0.8	12.58 ± 0.56	”
Off-field 5	0.5 ± 0.7	1.80 ± 0.37	”	1.16 ± 0.16	⋯	⋯	2.3 ± 0.6	10.59 ± 0.56	”

Notes.
[a] Normalization of the Gaussian at the fixed center energy $E = 0.525$ keV in units of L.U. (photons s^{-1} cm^{-2} str^{-1}).
[b] The EM for the foreground (LB+SWCX) component with temperature fixed at $kT = 0.1$ keV.
[c] Temperature of Galactic halo warm-hot phase thermal component.
[d] Temperature of Galactic halo hot phase thermal component.
[e] The Ne abundance for the Galactic halo warm-hot phase component.
[f] Normalization of the power-law model with fixed photon index $\Gamma = 1.52$ in units of photons keV^{-1} s^{-1} sr^{-1} cm^{-2}.
[g] Galactic halo one-temperature model.
[h] Galactic halo two-temperature model.
[i] Galactic halo one-temperature model with variable Ne abundance.

Table 4). Therefore, we performed global fits, simultaneously fitting all four spectra for the $1T$, $2T$, and $1T_{\rm Ne}$ models. We tied the temperature of the warm-hot component and allowed the normalization to vary among different fields. We also allowed all other free model parameters among the observations to vary.

The resulting warm-hot phase temperature was 0.198 ± 0.007 keV for the $1T$ and $1T_{\rm Ne}$ and 0.176 ± 0.008 keV for the $2T$ models. The warm-hot phase EMs are in the range of $(0.7–1.8) \times 10^{-2}$ cm^{-6} pc. The hot component has temperatures and EMs in the range of 0.65–0.90 keV and $(0.4–1.0) \times 10^{-3}$ cm^{-6} pc, respectively. In the $1T_{\rm Ne}$ model, the Ne abundances are in the range of 1.4–4.0 times solar. The hot component or the overabundance of Ne are required at a significance of more than 4σ (F-test probability of >99.99%; $2T$ model: $\Delta\chi^2 = 61.6$, $\Delta{\rm dof} = 8$; $1T_{\rm Ne}$ model: $\Delta\chi^2 = 44.6$, $\Delta{\rm dof} = 4$). The simultaneous fit parameters are reported in Table 5.

4.2. Point-source Contribution

To estimate the contribution of point sources to empty field observations, we have extracted the combined spectrum of all sources detected in each Suzaku field of view. For the background spectrum, we used the diffuse emission spectrum extracted from the entire field after removing the detected sources. The background was scaled by the ratio of the total area of the sources to the area of diffuse background. The point sources occupy about 30%–40% of the area of the entire field of view in our observations.

We fitted the cumulative point-source spectrum for each field with an absorbed power law. The best-fit power-law photon indices vary from 1.98 to 2.69 in our fields. The spectrum of the sources identified in Off-field 3 shows an excess emission over a power law around 1 keV. The excess is fitted well with a thermal component with temperature $T = 1.02$ keV and 0.5–2.0 keV flux of 1.8×10^{-13} erg s^{-1} cm^{-2}. This excess thermal component could be due to Milky Way stellar sources. Many stars are known to have two-temperature thermal spectra, a hot active component at a nominal temperature of $kT_a \sim 1$ keV, and a comparatively cooler quiescent component at $kT_q \sim 0.3$ keV (Kashyap et al. 1992). Gupta & Galeazzi (2009) studied the point-source X-ray emission identified in the high-latitude XMM-Newton fields. The authors also noted similar thermal component emission with a temperature $T = 0.92$ keV and attributed it to the stellar hot active component.

In our fields, the total 0.5–2.0 keV surface brightnesses (SBs) of the X-ray background (diffuse+resolved point sources) are 2.2×10^{-11}, 1.5×10^{-11}, 1.6×10^{-11}, and 1.6×10^{-11} erg s^{-1} cm^{-2} deg^{-2} along Off-field 2, Off-field 3, Off-field 4, and Off-field 5, respectively. We measured point-source SBs of 3.3×10^{-12}, 2.0×10^{-12}, 2.2×10^{-12}, and 9.7×10^{-13} erg s^{-1} cm^{-2} deg^{-2}, which correspond to 6%–15% of the total SB of an empty field emission. Thus, it is unlikely that the details of the point-source subtraction process have biased our results in any way.

5. Discussion

5.1. Hot or Ne Overabundant Phase of the CGM

In three out of our four Suzaku observations, we have detected excess soft X-ray emission near 0.8–1.0 keV. We used

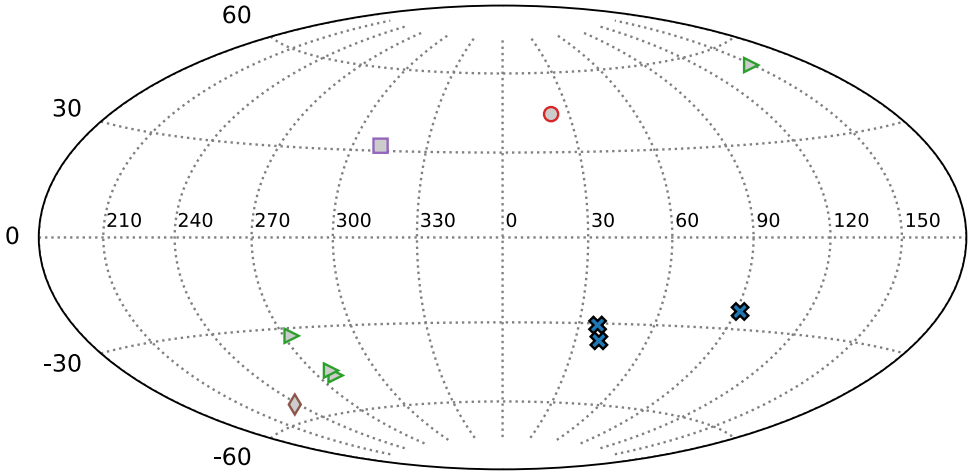

Figure 3. Sky map showing the locations of the sight lines with detections of the hot component of the CGM and/or Ne overabundant warm-hot gas. The sight lines shown with blue crosses are from this work, the red circle is from Das et al. (2019a, 2019b), the green triangles are from Yoshino et al. (2009), the purple square is from Mitsuishi et al. (2012), and the brown diamond is from Henley & Shelton (2013). The Galactic center is at the center of the plot. The figure shows that the presence of the hot component and/or Ne overabundance is not necessarily associated with the structures at the Galactic center, such as the FB.

two different models to fit this excess emission. We found that this excess emission is either from the hot gas at temperatures near 0.65–0.90 keV with a EM of $(1.0 \pm 0.4) \times 10^{-3}$ cm^{-6} pc or from an enhanced Ne abundance of 1.5–4.0 solar in the warm-hot gas in the Galactic CGM. The temperature of the hot phase is similar to the recently discovered hot component in the Milky Way CGM by Das et al. (2019a, 2019b). Using very high signal-to-noise XMM-Newton absorption and emission spectra in the sight line of blazar 1ES 1553+113, Das et al. discovered the hot ∼0.86 keV gas coexisting with the warm-hot ∼0.09 keV gas in the Galactic CGM. This was a robust detection, and it was the first time that the hot component was detected both in emission and absorption. The 1ES 1553+113 sight line passes close to the X-ray shell around the Fermi bubble (FB); while Das et al. concluded that, in absorption, the hot gas is unlikely to be associated with the FB, this possibility could not be ruled out for the hot phase detected in emission. Das et al. also noted nonsolar abundance ratios and alpha-enhancement of light metals, N, O, and Ne, in the warm-hot phase, similar to our Ne overabundance.

A few earlier Suzaku and XMM-Newton X-ray emission studies also reported suggestive evidence of a higher-temperature (0.5–0.9 keV) or enhanced Ne abundance in the Galactic halo. Ursino et al. (2016) reported an excess emission around 0.9 keV toward the inner region of the North Polar Spur (NPS)/Loop1 structure. They probed the region using Suzaku shadow observations of the high column density cloud MBM36 and a nearby empty region. The authors modeled this excess emission with the Ne overabundance [Ne/O = 1.7] or an absorbed hotter thermal component at $kT = 0.76$ keV with an EM of 1.7 ± 0.6^{-3} cm^{-6} pc. Since this sight line probes the NPS/Loop1 structure, they associated this excess emission with the shell of a superbubble predicted by some NPS models. Our measured hotter halo component temperatures/EMs or enhanced Ne abundances are in the same range as observed by Ursino et al. (2016).

Yoshino et al. (2009) analyzed the soft diffuse X-ray emission of 13 high-latitude Suzaku fields. For their preferred model, they used variable Fe and Ne abundances for the Galactic halo thermal emission. They measured an average temperature of 0.216 ± 0.017 keV and Fe/O and Ne/O ratios of 0.51–2.99 and 0.91–3.79, respectively. They fitted spectra toward four sight lines with supersolar Fe and Ne abundances with an alternative model of an additional higher-temperature (0.5–0.9 keV) emission component with solar abundances (similar to our 2T model). Their measured EMs of a higher-temperature component of $(5.0–9.5) \times 10^{-4}$ cm^{-6} pc or Ne/O ratios of 0.91–3.79 are in the same range as our values.

Henley & Shelton (2013) also reported the detection of a high halo temperature ($T \approx 0.86$ keV) toward one sight line (No. 83; their Table 1) and some excess emission around ≈1 keV in some other sight lines. For the No. 83 sight line, they used a 2T model, with one thermal component to model the excess emission around ≈1 keV and one to model the 0.17–0.26 keV emission. The authors did not report on such excess emission in other sight lines.

In Figure 3, we have plotted all of these observations on the sky map, which shows a widespread prevalence of the hot component of the CGM and/or Ne overabundance. Our sight lines are also far from the NPS/Loop1 structure or the FB, suggesting that the presence of the hot component or nonsolar enhanced Ne gas is not necessarily associated with these special structures in the Galactic center.

5.2. Very Bright Warm-hot Phase of the CGM

The average temperature of the warm-hot phase of the CGM that we measure, ≈0.2 keV, is close to the Milky Way virial temperature and in agreement with previous studies of the Galactic halo X-ray emission. However, our measured EMs are excessively high ($(1.13–1.74) \times 10^{-2}$ cm^{-6} pc) along Off-field 2, Off-field 4, and Off-field 5. Off-field 2 was also observed with XMM-Newton in 2014, and we found a similarly high EM of $\sim 1.65 \times 10^{-2}$ cm^{-6} pc (Gupta et al. 2017).

Henley & Shelton (2015) measured Galactic halo EMs in the range of $(2.2–6.7) \times 10^{-3}$ cm^{-6} pc[12] using the XMM-Newton and/or Suzaku shadow observations toward six sight lines. Henley & Shelton (2013) studied the halo emission along 110 high-latitude XMM-Newton sight lines and found that the EM

[12] For their LB foreground model and the Anders & Grevesse (1989) abundances; same as our 1T model.

varies by over an order of magnitude ((0.4–7) $\times 10^{-3}$ cm^{-6} pc with a median detection of 1.9×10^{-3} cm^{-6} pc). Our measured CGM EMs toward three fields are significantly higher than these values.

Recently, using the HaloSat data, Kaaret et al. (2020) found similarly high values of the warm-hot CGM EMs, (1.1–1.4) $\times 10^{-2}$ cm^{-6} pc (converting their EMs to EMs for solar abundances), toward the inner halo. Kaaret et al. measured a Galactic halo temperature and EM of 0.20 keV and 1.26×10^{-2} cm^{-6} pc, respectively, in one of their fields close to our Off-field 5 sight line. This suggests that the excessively high EMs are associated with the inner halo. In 2020 December, when we were revising this paper after the referee comments, a newly published sky map from the first eROSITA all-sky survey reported the discovery of large (∼14 kpc above and below the Galactic center) soft X-ray–emitting bubbles (Predehl et al. 2020). The high EMs toward our fields could also be a result of the contribution from these bubbles. Our sight lines of Off-field 2 and Off-field 5 pass through the southern bubble, and the Off-field 4 sight line passes close to the outer boundary of the northern bubble. We will investigate this further in a subsequent paper (A. Gupta et al. 2021, in preparation).

6. Conclusion

In this work, we present the soft X-ray emission properties of the Galactic CGM along four directions using Suzaku and Chandra observations. We have found strong O I contamination in the Suzaku data using standard filtering for the elevation angle from the bright Earth limb of larger than DYE_ELV > 20°. We carefully investigated the effect of O I contamination and found that with DYE_ELV > 40°, O I emission can be reduced significantly, and a good balance is struck between the loss of exposure time and O I contamination. To model the residual O I emission, we included Gaussian emission at 0.525 keV in the spectral modeling.

We clearly detect the emission from the warm-hot CGM of the Milky Way in all four sight lines. The measured temperature of ≈0.2 keV (2.1×10^6 K) is close to the Galaxy's virial temperature, consistent with previous studies. However, the EMs are very high toward three sight lines probing the inner halo. These high EMs are in line with the recent HaloSat results (Kaaret et al. 2020).

Toward three sight lines, we have detected excess emission near 0.8–1.0 keV. There are two possibilities to explain this excess emission. It may arise from a hotter component of the Galactic CGM at a temperature of about 0.65–0.90 keV. The temperature of this hotter component is similar to that recently discovered (∼0.86 keV) by Das et al. (2019a, 2019b) toward the sight line to blazar 1ES 1553+113. Detection of X-ray emission from the hot CGM in our Suzaku fields suggests that the 1ES 1553+113 sight line is not unique and the hot phase of the Galactic CGM is more widespread. Alternatively, the excess emission could be a signature of overabundance of Ne in the warm-hot phase of the Galactic CGM. The variable Ne abundance model required Ne/O abundances of 1.5–3.4 solar; this is also not unprecedented (Section 5.1). Both models of the excess emission have similar statistical significance, so we do not prefer one over the other. Future missions like XRISM and Athena with better spectral resolution may able to differentiate the two models.

Whether the excess emission is from the hot gas or overabundant Ne, it poses a challenge to galaxy formation and evolution models. Literature on supervirial temperature and/or nonsolar abundance ratios in the CGM is limited. Multistage feedback can produce the hot component, as suggested by the theoretical models of Tang et al. (2009). As discussed in Das et al., the nonsolar Ne/O abundance ratio may be informative of the depletion of metals like oxygen. Recently, van de Voort et al. (2021) studied the effect of magnetic fields on a simulated galaxy and its CGM. Their results show that magnetic fields in the galaxy's halo can cause inhomogeneous mixing; this might lead to apparent nonsolar abundance ratios. Understanding the origin of the supervirial hot component and/or nonsolar abundance ratios of the Milky Way CGM is going to be of interest for theoretical models of the CGM.

We thank the anonymous referee for the useful comments that helped improve the paper. We gratefully acknowledge support through NASA ADAP grant 80NSSC18K0419 to A.G. Support for this work was also provided by the National Aeronautics and Space Administration through Chandra Award No. GO9-20077X to A.G. issued by the Chandra X-ray Observatory Center, which is operated by the Smithsonian Astrophysical Observatory for and on behalf of the National Aeronautics and Space Administration under contract NAS8-03060. S.M. gratefully acknowledges NASA grant NNX16AF49G. Y.K. acknowledges support from PAPIIT grant IN106518 and PAPIIT-PASPA.

ORCID iDs

Anjali Gupta https://orcid.org/0000-0003-1880-1474
Joshua Kingsbury https://orcid.org/0000-0002-2302-6305
Smita Mathur https://orcid.org/0000-0002-4822-3559
Sanskriti Das https://orcid.org/0000-0002-9069-7061
Yair Krongold https://orcid.org/0000-0001-6291-5239
Fabrizio Nicastro https://orcid.org/0000-0002-6896-1364

References

Anders, E., & Grevesse, N. 1989, GeCoA, 53, 197
Cappelluti, N., Li, Y., Ricarte, A., et al. 2017, ApJ, 837, 19
Das, S., Mathur, S., Gupta, A., Nicastro, F., & Krongold, Y. 2019a, ApJ, 887, 257
Das, S., Mathur, S., Nicastro, F., & Krongold, Y. 2019b, ApJL, 882, L23
Dickey, J. M., & Lockman, F. J. 1990, ARA&A, 28, 215
Fang, T., Buote, D., Bullock, J., & Ma, R. 2019, ApJS, 217, 21
Galeazzi, M., Gupta, A., & Ursino, E. 2009, ApJ, 695, 1127
Gupta, A., & Galeazzi, M. 2009, ApJ, 702, 270
Gupta, A., Galeazzi, M., Koutroumpa, D., Smith, R., & Lallement, R. 2009, ApJ, 707, 644
Gupta, A., Mathur, S., Galeazzi, M., & Krongold, Y. 2014, Ap&SS, 352, 775
Gupta, A., Mathur, S., & Krongold, Y. 2017, ApJ, 836, 243
Gupta, A., Mathur, S., Krongold, Y., Nicastro, F., & Galeazzi, M. 2012, ApJL, 756, L8
Henley, D., Shelton, R., Kwak, K., Joung, M. R., & Mac Low, M. 2010, ApJ, 723, 935
Henley, D. B., & Shelton, R. L. 2013, ApJ, 773, 92
Henley, D. B., & Shelton, R. L. 2015, ApJ, 808, 22
Kaaret, P., Koutroumpa, D., Kuntz, K. D., et al. 2020, NatAs, 4, 1072
Kashyap, V., Rosner, R., Micela, G., et al. 1992, ApJ, 391, 667
Lehmer, B. D., Xue, Y. Q., Brandt, W. N., et al. 2012, ApJ, 752, 46
Liu, W., Chiao, M., Collier, M. R., et al. 2017, ApJ, 834, 33
Mitsuishi, I., Gupta, A., Yamasaki, N. Y., et al. 2012, PASJ, 64, 18
Nakashima, S., Inoue, Y., Yamasaki, N., et al. 2018, ApJ, 862, 34
Nelson, D., Kauffmann, G., Pillepich, A., et al. 2018, MNRAS, 477, 450
Nicastro, F., Zezas, A., Drake, J., et al. 2002, ApJ, 573, 157
Oppenheimer, B. D., Crain, R. A., Schaye, J., et al. 2016, MNRAS, 460, 2157
Predehl, P., Sunyaev, R. A., Becker, W., et al. 2020, Natur, 588, 227
Sekiya, N., Yamasaki, N. Y., Mitsuda, K., & Takei, Y. 2014, PASJ, 66, L3

Smith, R. K., Bautz, M. W., Edgar, R. J., et al. 2007, PASJ, 59, S141
Smith, R. K., Brickhouse, N. S., Liedahl, D. A., & Raymond, J. C. 2001, ApJL, 556, L91
Snowden, S. L., Egger, R., Finkbeiner, D. P., Freyberg, M. J., & Plucinsky, P. P. 1998, ApJ, 493, 715
Snowden, S. L., Freyberg, M. J., Kuntz, K. D., & Sanders, W. T. 2000, ApJS, 128, 171
Stinson, G. S., Brook, C., Prochaska, J. X., et al. 2012, MNRAS, 425, 1270
Tang, S., Wang, Q. D., Lu, Y., & Mo, H. J. 2009, MNRAS, 392, 77
Ursino, E., Galeazzi, M., & Liu, W. 2016, ApJ, 816, 33
van de Voort, F., Bieri, R., Pakmor, R., et al. 2021, MNRAS, 501, 4888
Wang, Q. D., Yao, Y., Tripp, T. M., et al. 2005, ApJ, 635, 386
White, S. D. M., & Rees, M. J. 1978, MNRAS, 188, 341
Williams, R. K., Mathur, S., Nicastro, F., et al. 2005, ApJ, 631, 856
Williams, R. K., Mathur, S., Nicastro, F., et al. 2006a, ApJ, 642L, 95
Williams, R. K., Mathur, S., & Nicastro, F. 2006b, ApJ, 645, 179
Williams, R. K., Mathur, S., Nicastro, F., et al. 2007, ApJ, 665, 247
Yoshino, T., Mitsuda, K., Yamasaki, N. Y., et al. 2009, PASJ, 61, 805